Review of Scientific Instruments

RESEARCH ARTICLE | OCTOBER 05 2023

A 1.25-GHz multi-amplitude modulator driver in 0.18 μm SiGe BiCOMOS technology for high speed quantum key distribution

Zhao-Yuan Chen ; Chen-Xi Zhu ; Zhi-Sheng Huang ; Yang Li ; Xin-Zhe Wang ; Fu-Tian Liang ; Ge Jin; Wen-Qi Cai; Sheng-Kai Liao ; Cheng-Zhi Peng

Check for updates

Rev. Sci. Instrum. 94, 104703 (2023)
https://doi.org/10.1063/5.0167218

View Online
Export Citation
CrossMark

Articles You May Be Interested In

A functional integral formalism for quantum spin systems

J. Math. Phys. (July 2008)

Modes selection in polymer mixtures undergoing phase separation by photochemical reactions

Chaos (June 1999)

Spreading of a surfactant monolayer on a thin liquid film: Onset and evolution of digitated structures

Chaos (March 1999)

06 October 2023 01:32:00

500 kHz or 8.5 GHz?
And all the ranges in between.
Lock-in Amplifiers for your periodic signal measurements



Find out more
Zurich Instruments

AIP Publishing

Review of Scientific Instruments ARTICLE pubs.aip.org/aip/rsi

A 1.25-GHz multi-amplitude modulator driver in 0.18 μm SiGe BiCOMOS technology for high speed quantum key distribution

Cite as: Rev. Sci. Instrum. 94, 104703 (2023); doi: 10.1063/5.0167218
Submitted: 11 July 2023 • Accepted: 18 September 2023 •
Published Online: 5 October 2023

View Online Export Citation CrossMark

Zhao-Yuan Chen,[1,2,3,4] Chen-Xi Zhu,[5] Zhi-Sheng Huang,[6] Yang Li,[1,2,3] Xin-Zhe Wang,[2,3,a)] Fu-Tian Liang,[1,2,3] Ge Jin,[3,6] Wen-Qi Cai,[1,2,3] Sheng-Kai Liao,[1,2,3,5,a)] and Cheng-Zhi Peng[1,2,3]

AFFILIATIONS

[1] Hefei National Research Center for Physical Sciences at the Microscale and School of Physical Sciences, University of Science and Technology of China, Hefei 230026, China
[2] Shanghai Research Center for Quantum Science and CAS Center for Excellence in Quantum Information and Quantum Physics, University of Science and Technology of China, Shanghai 201315, China
[3] Hefei National Laboratory, University of Science and Technology of China, Hefei 230088, China
[4] PLA Rocket Force University of Engineering, Xi'an 710025, China
[5] School of Cyberspace Security, University of Science and Technology of China, Hefei 230026, China
[6] Department of Modern Physics, University of Science and Technology of China, Hefei 230026, China

[a)] **Authors to whom correspondence should be addressed:** wxzyf@ustc.edu.cn and skliao@ustc.edu.cn

ABSTRACT

Quantum key distribution (QKD) research has yielded highly fruitful results and is currently undergoing an industrialization transformation. In QKD systems, electro-optic modulators are typically employed to prepare the required quantum states. While various QKD systems operating at GHz repetition frequency have demonstrated exceptional performance, they predominantly rely on instruments or printed circuit boards to fulfill the driving circuit function of the electro-optic modulator. Consequently, these systems tend to be complex with low integration levels. To address this challenge, we have introduced a modulator driver integrated circuit in 0.18 μm SiGe BiCMOS technology. The circuit can generate multiple-level driving signals with a clock frequency of 1.25 GHz and a rising edge of ~50 ps. Each voltage amplitude can be independently adjusted, ensuring the precise preparation of quantum states. The measured signal-to-noise ratio was more than 17 dB, resulting in a low quantum bit error rate of 0.24% in our polarization-encoding system. This work will contribute to the advancement of QKD system integration and promote the industrialization process in this field.

Published under an exclusive license by AIP Publishing. https://doi.org/10.1063/5.0167218

06 October 2023 01:32:00

I. INTRODUCTION

The growth of quantum computing presents challenges for information security and privacy. Quantum key distribution (QKD)[1] offers a physically secure alternative to classical communication methods by leveraging quantum mechanics. Over the past few years, QKD has made significant progress in key distribution, with distance increased from tens of centimeters to thousands of kilometers[2–7] and experiments moving from controlled laboratory settings to real-world applications.[8–16] Satellite-based long-distance key distribution and key relay, as well as quantum communication networks based on intercity optical fiber networks, have been successfully tested multiple times.[17–24] The field of QKD is transitioning from the laboratory to reality with the emergence of the quantum communication industry.

To achieve the industrialization and commercialization of QKD, research efforts will focus on improving communication speed, increasing communication distance, and reducing costs. Reference 25 presents a blueprint for a large-scale integrated space-to-ground quantum communication network. Meeting the demand for a large-scale communication network requires a significant number of QKD terminal devices. Developing QKD devices with

Published under an exclusive license by AIP Publishing

integrated chips would not only meet the production capacity advantage for large-scale demand but also increase consistency and system integration in device research and development, which is crucial for QKD industrialization.

In QKD systems, quantum states typically require multi-dimensional encoding. For example, in the standard BB84 and measurement-device-independent (MDI) protocols,[1,2,5,26] at least four states need to be encoded. In some other protocols, such as the simplified BB84,[27,28] differential phase shift (DPS),[29,30] and coherent-one-way (COW)[31,32] protocols, only three or two states need to be encoded. Therefore, a four-amplitude driving signal can cover the general requirements of QKD applications with only one modulator. Unlike the PAM4 modulation method,[33] the QKD modulator requires a multi-amplitude modulation signal with lower noise, jitter, and higher amplitude to prepare high-extinction-ratio quantum states. In addition, each amplitude of the signal needs to be independently tunable to achieve precise quantum state manipulation. Currently, research in the QKD field generally uses instrument equipment such as anarbitrary waveform generator (AWG)[34,35] or printed circuit board (PCB)[36,37] with separate electronic components to generate the necessary driving signals. However, underpinned by silicon photonics technology, research in QKD transmitters is trending toward chipization and integration. As a result of this trend, separate electronic components and instruments occupy most of the volume and weight of QKD terminal equipment, which prevents them from taking advantage of the integration benefits of integrated photonics chips. In 2022, Zhu *et al.* designed a dedicated integrated driver chip for quantum state encoding in QKD systems and completed experimental verification.[38] However, due to the limited bandwidth of the driving signal, the system clock can only be limited to a few hundred MHz. At present, QKD systems based on photonics integrated chips mostly use clock frequencies above GHz to acquire a higher secure key rate.[39–41] However, there is less research on specific driver chips for high-speed QKD systems with frequencies above GHz. In the current process of industrializing QKD, there is an urgent need for an integrated driver chip with high bandwidth and low jitter to meet the requirements of high-speed QKD systems.

Therefore, this article carries out application-specific integrated circuit (ASIC) research for high-speed and integrated QKD terminal application scenarios. A driver chip for the modulator in a QKD system is designed. Combined with the silicon photonics QKD transmitter chip, the driving performance of the driver chip is verified, demonstrating the feasibility of supporting a 1.25 GHz QKD system. This work provides a reference for the development of high-speed and integrated QKD systems and further promotes the industrialization process of QKD.

II. CHIP DESIGN

A. Requirements

The QKD protocol requires the preparation of quantum states under different basis. The standard BB84 protocol typically encodes four quantum states. Therefore, it is required that the modulator driver can output four pulse signals of different amplitudes. Different from PAM4 encoding in classical optical communication, QKD requires very high precision in quantum state encoding. On the one hand, each amplitude of the modulated signal needs to be independently adjustable to meet the accuracy of quantum state preparation. These two points are essential to achieving a low quantum bit error rate.

Figure 1(a) is a simulated eye diagram of PAM2 optical communication (PAM4 works in the same way). Since the optical extinction ratio (OER) in typical optical communication is 4–6 dB,[33] for a modulator with a 4 V half-wave voltage, only 1.5 V amplitude signals are needed to drive it. In addition, as shown in the figure, there is a threshold to distinguish between 0 and 1 during decoding. As long as the noise is within the threshold (i.e., eyes are open), it will not cause error bits. Driving signals with an electrical signal-to-noise ratio (ESNR) of 11.8 dB will lead to a bit error rate (BER) of about 1×10^{-12}, which is low enough to meet communication needs. However, in the BB84, DPS, and MDI schemes,[27,29,30,41] π-phase modulation is required to obtain the maximum extinction ratio and reduce QBER as much as possible. The required drive signal

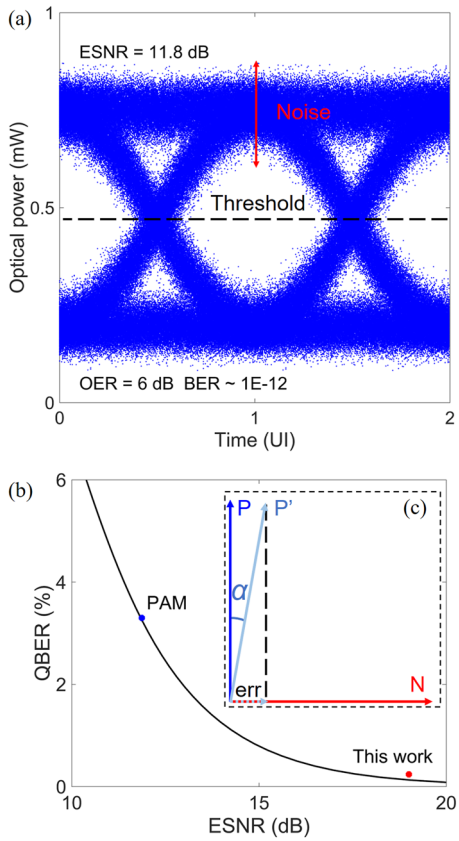


FIG. 1. (a) Eye diagram of PAM optical communication. ESNR is the electrical signal-to-noise ratio of the driving signal. OER is the optical extinction ratio of the modulated optical signal. BER is the estimated bit error rate. (b) Quantum bit error rate (QBER) under different ESNRs. The blue dot is QBER simulated using an ESNR of 11.8 dB. The red dot represents QBER and ESNR achieved in this work. (c) Schematic diagram of the polarization encoding QKD principle. P and N are ideal quantum state vectors under the X basis. P′ represents the actual prepared P state, with an angle α between it and the ideal state due to the noise of driving signals. err is the projection vector of P′ on the N state, representing the error code.

06 October 2023 01:32:00

Published under an exclusive license by AIP Publishing

amplitude needs to reach more than the half-wave-voltage of the Mach–Zehnder modulator (MZM). Figure 1(c) is a schematic diagram of polarization encoding QKD. P and N are ideal quantum states, while P′is the actual prepared P state due to the noise of driving signals. Unlike optical communication, there is no concept of threshold in the QKD decoding process. Any slight angular deviation between P′and P will project an err vector onto the N state and introduce error bits. Therefore, the noise of the driving signal must be low enough to achieve a low quantum bit error rate (QBER). Figure 1(b) is the simulated QBER under different ESNRs. (The calculation process is in the Appendix.) Obviously, directly applying PAM to QKD applications will result in a very high QBER. In order to reduce the QBER to less than 1%, it is necessary to increase the ESNR to more than 15 dB.

B. Modulator driver

For the four polarization states and three intensity state optical signals required by the decoy state QKD protocol, the driver chip corresponding to the silicon photonics modulator needs to be able to randomly generate four or three different amplitudes of Giga-Hz system frequency electrical pulse signals. In this thesis, the multi-amplitude output is realized by one-hot gating of three channels, which means that at most only one channel can be opened with a certain code. Figure 2 shows the overall block diagram of the modulator driver chip. Each channel consists primarily of a receiver module[42] that receives encoded signals from the logic control terminal, a pulse width control (PWC) module[43] that provides a pulse width fine-tuning range of ±35 ps, a predriver module that amplifies the driving capability of the pulse signals, and an output module that outputs multiple amplitude current pulses, which are amplified by an off-chip power amplifier to drive the electro-optical modulator. Considering the incoherence between different modulation states and the nonlinearity of the electro-optical modulator, each of the output amplitudes can be adjusted individually and continuously. Since the amplitude jitter of the driving electrical signal directly affects the extinction ratio of the laser signal, the driver chip adopts differential signal transmission. To reduce reflections, one of the differential outputs is matched both on the source side and terminal side, while the other one is matched by two 50 Ω pull-up resistors within the chip.

1. Predriver module

The high currents (up to 60 mA) driven by the output stage require large differential transistors, resulting in large input capacitance. If the differential pair of the output stage is driven directly, the bandwidth of the signal path will be significantly reduced. Therefore, most SiGe-based drive circuits are pre-amplified using multi-stage cascaded emitter followers.[44,45] The amplified signal is then transmitted to the final output stage, which maintains high bandwidth, reduces the output resistance of the output stage transistor, and increases the breakdown voltage.[46] However, the main disadvantages of multi-stage cascaded emitter followers are the high supply voltage requirements, high current consumption, and large signal overshoot.[47,48] The magnitude of the overshoot depends mainly on the emitter follower's tail current and its base's equivalent drive impedance. When one transistor of the differential load pair at the next stage is switched on, the base current is injected by the power supply through the emitter follower, while the other one is turned off, and the base current is discharged through a fixed tail current source. Since the drive current required to turn on an npn device is much lower than the discharge current required to turn it off, an excessive turn-on current will introduce a large overshoot and unnecessary power dissipation when the required discharge current is reached. To avoid this situation, a differential pair of switches is adopted to dynamically provide the excess discharge current for the turn-off transistor.[49]

06 October 2023 01:32:00

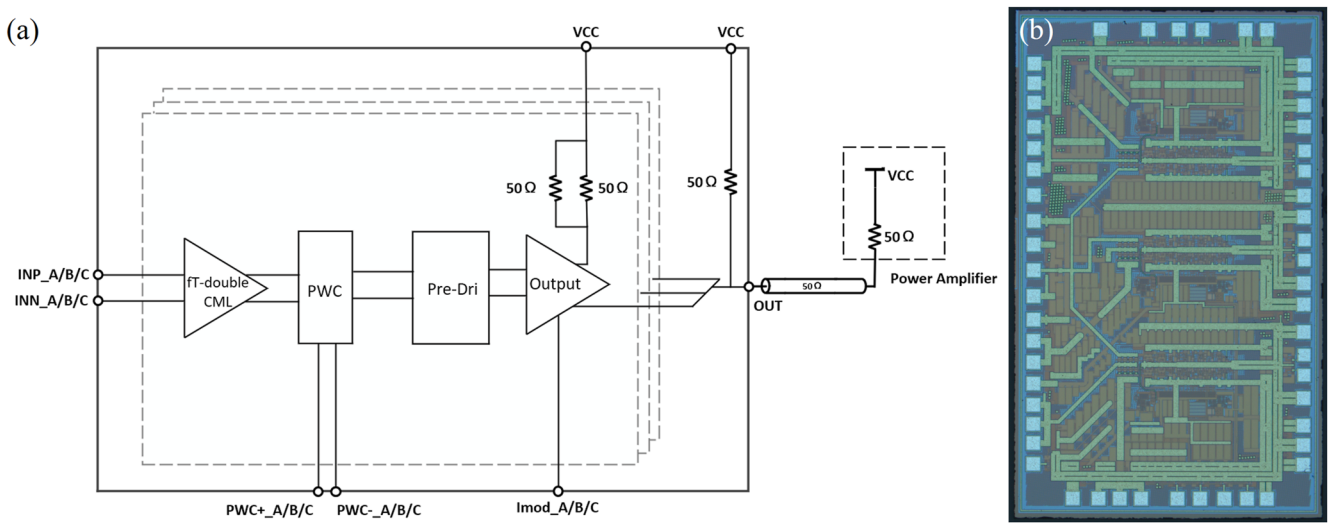


FIG. 2. (a) Structure of the modulator driver. The modulation driver consists of three independent pulse generator channels, which convert the three-channel input digital pulse signal into an analog pulse signal with multiple adjustable amplitudes. Each amplitude can be adjusted individually. (b) A microscopic picture of the chip.

Published under an exclusive license by AIP Publishing

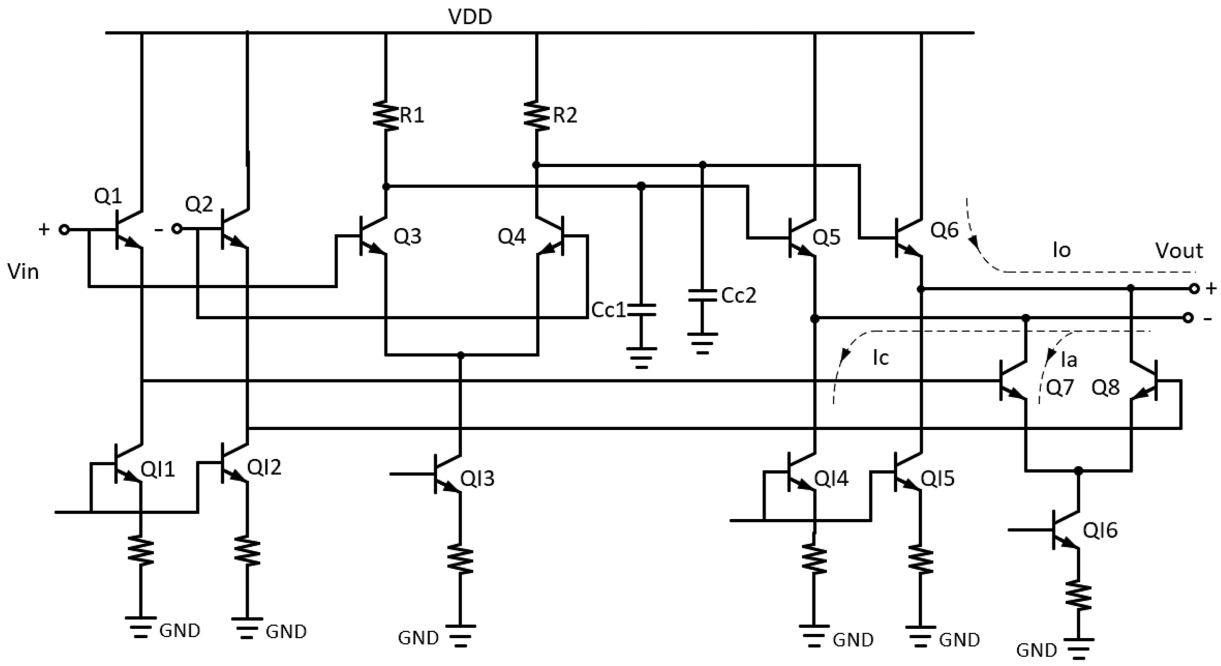


FIG. 3. Schematic of a dynamic emitter-follower buffer in the predriver module. Emitter follower transistors Q5 and Q6 provide level shifting and current gain to drive the output stage, while an additional pair of switches, Q7 and Q8, is used to reduce overshoot.

Figure 3 shows a schematic diagram of a dynamic emitter-follower buffer. Cc is a compensation capacitor connected in parallel at the input stage of the emitter follower to damp ringing.[48] When the load transistor is turned off, the discharge current is the sum of currents I_c and I_a, where I_a is dynamically supplied by the differential switches Q7 and Q8. By adjusting the value of I_a, a balance between the small turn-on current and the large turn-off current is achieved, and the peak current of the base and collector of the emitter follower is reduced. Furthermore, since the output impedance of Q7 and Q8 is about the reciprocal of the transconductance of the emitter followers Q5 and Q6, V_{out} is a low-impedance node, so Q7 and Q8 have a short time constant and switch first before the differential pair of Q3 and Q4 in the main data path, which ensures the effective operation of the circuit. In this thesis, three cascaded dynamic emitter followers are adopted as the predriver module to pre-amplify the pulse signals to an adequate magnitude for the final output stage at high bandwidth.

2. Output module

As shown in Fig. 4(a), the output stages of three channels are connected with a wire-AND. In response to a randomly coded one-hot stimulus from the control terminal, the output pulse signals with four magnitudes (including the zero magnitudes when all three channels are deselected) are amplified by an off-chip power amplifier to the modulation voltages required by the electro-optical modulator. Each channel corresponds to an independently adjustable voltage.

Figure 4(b) shows the internal circuit diagram of the output stage in one channel. The output magnitude can be adjusted continuously by changing the bias voltage V_{adj} of the tail current source. A feedback operational amplifier is adopted to provide better linearity for amplitude regulation. A small resistor, RE, is introduced in series with the emitter of the switching transistor, providing a large voltage drop at rapidly changing large currents.[50] Due to negative feedback, the large voltage drop slows down the forward bias phenomenon of the emitter junction, thereby reducing the secondary breakdown problem caused by overheating at high currents. Since the I_{adj} has a wide adjustment range (10–60 mA), a small resistor RE is introduced in series at the emitter of the switching transistor, and RE has a large voltage drop at rapidly changing large current values. Due to the negative feedback, the large voltage drop slows down the forward bias phenomenon of the emitter junction, thereby reducing the secondary breakdown problem caused by overheating at high currents.[51]

III. CHIP IMPLEMENTATION AND CHARACTERIZATION

The chip was manufactured using 180 nm SiGe BiCMOS technology, which incorporates high-performance npn heterojunction bipolar transistors (HBTs) capable of achieving transit frequencies of up to 240 GHz. The chip has a compact size of 1.35×2.25 mm^2, as illustrated in Fig. 2(b). To evaluate the chip's performance, we conducted tests on the output signal both before and after amplification, operating at a clock frequency of 1.25 GHz. Additionally, we performed a modulation experiment using the designed chip to drive

06 October 2023 01:32:00

Published under an exclusive license by AIP Publishing

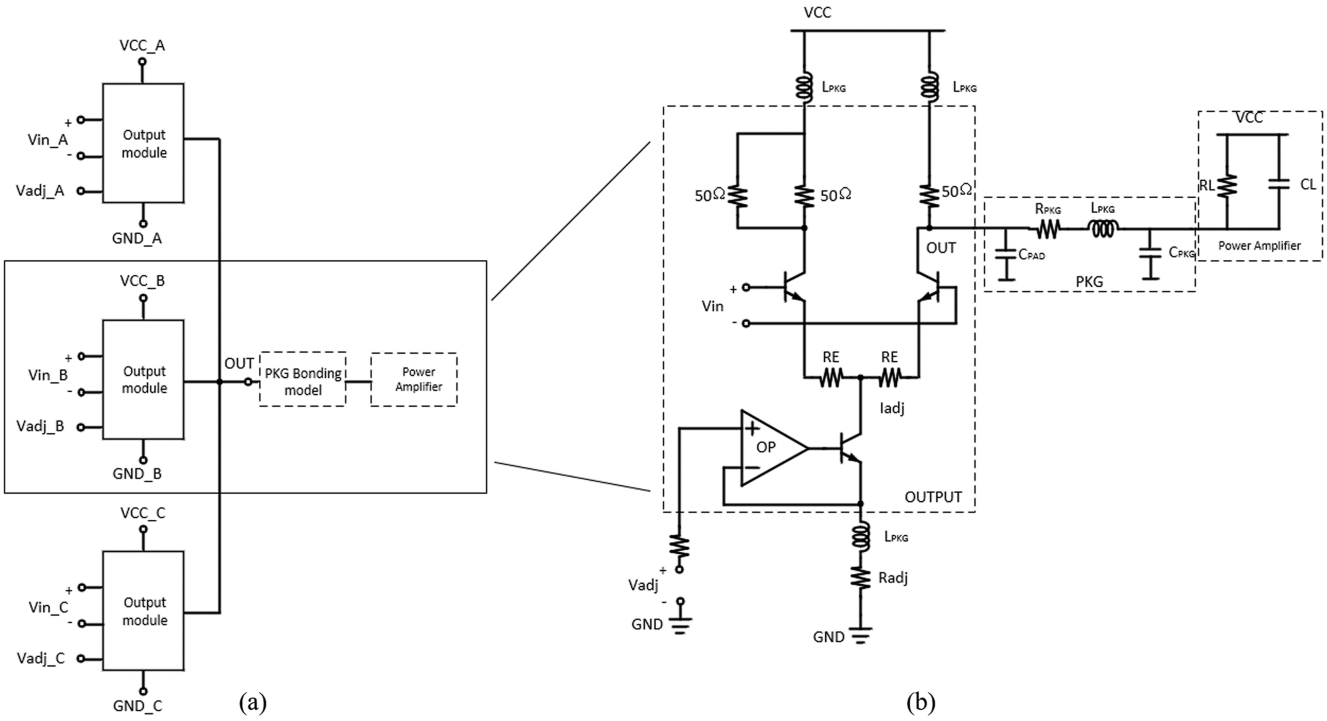


FIG. 4. (a) Schematic of output module. The output stages of the three channels are connected through a wire-AND to generate multi-amplitude pulses. (b) Detailed output structure diagram of one channel. RL, resistive load of the power amplifier; CL, capacitive load of the power amplifier; the suffix PKG is used to mark the parasitic resistance, capacitance, and inductance introduced into the package.

a silicon photonics QKD chip. The experimental setup, depicted in Fig. 5, involved an FPGA board for generating data signals for the driver chips and providing the clock signal for the receiving end. The modulator driver chip (MDC) receives three-channel current mode logic (CML) signals and produces a multi-amplitude driving signal. This driving signal is then amplified using an HMC659 chip before being input to a QKD photonics integrated chip (PIC) for polarization state encoding. The encoded photons are received at the QKD receiving end, where they are decoded by the decoding module

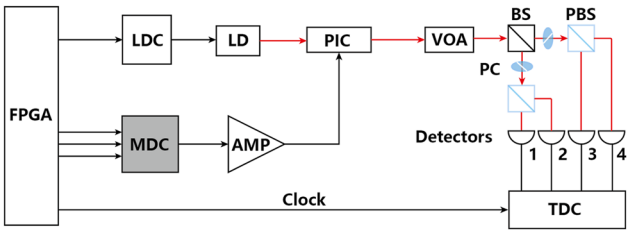


FIG. 5. Experimental setup. FPGA, field-programmable gate array; LDC, laser driver chip; MDC, the modulator driver chip designed in this work; LD, laser diode; AMP, amplifier; PIC, photonics integrated chip; VOA, variable optical attenuator; BS, beam spliter; PBS, polarization beam spliter; PC, polarization controller, TDC, time-to-digital converter. The black and red lines represent electrical and optical signals, respectively.

and detected by single photon detectors. A time-to-digital converter (TDC) records the arrival time of each photon, and coincidence counting is performed using the clock signal.

First, we utilized a Teledyne LeCroy LabMaster 10 Zi 36 GHz Systems oscilloscope with a 36 GHz analog bandwidth and 80 GSa/s to directly observe the output signal. By triggering the oscilloscope multiple times, we recorded over a thousand waveforms, which are plotted in Fig. 6. Figure 6(a) displays the eye diagram of the random RZ pattern pulse generated by the driver chip, while Fig. 6(b) shows the amplified signal by the HMC659 chip. The rising edge of the signal is marked in Fig. 6(a), taking ~50 ps to rise from 20% to 80%. Notably, the rising time remains unchanged after amplification. From the waveform data, we statistically obtained the signal amplitude, noise RMS, and ESNR, as detailed in Table I. The mean value and RMS value were calculated from the waveform data collected over a 200 ps range. To generate four quantum states, we adjusted the voltage of each amplitude to match the half-wave voltage of the PIC. The four amplitudes, namely no pulse, low pulse, medium pulse, and high pulse, were set to −0.062, −0.441, −0.755, and −1.414 V, respectively. The noise RMS was found to be less than 60 mV. Following amplification, the maximum pulse amplitude exceeded 6.5 V, with a noise RMS of 78 mV. The measured ESNR was determined to be 19.2 dB, surpassing the requirements outlined in the theoretical analysis section.

Then, we proceeded with a modulation experiment utilizing the designed chip to drive a silicon photonics QKD chip. As illustrated

06 October 2023 01:32:00

Published under an exclusive license by AIP Publishing

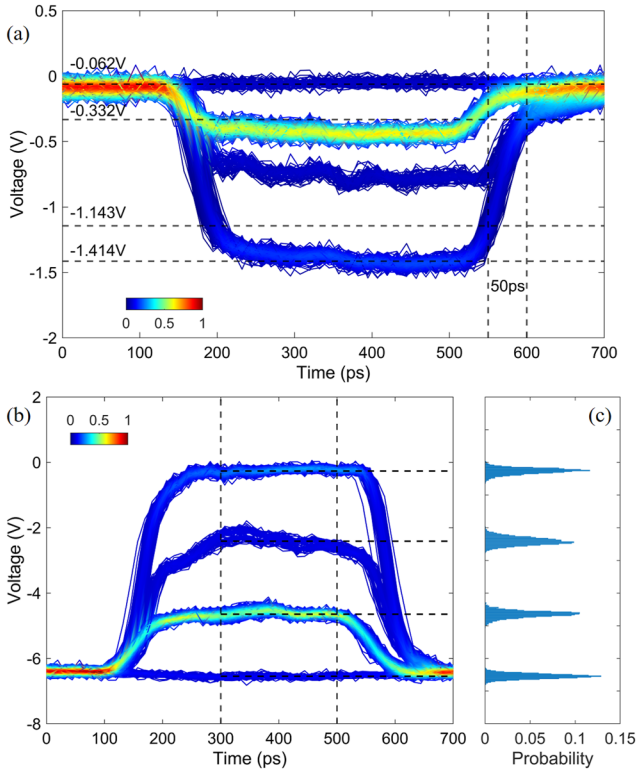


FIG. 6. (a) Chip output signal before amplification. The rise time of the signal from 20% to 80% is about 50 ps. (b) Amplified signal. We calculate the signal amplitude and noise from 300 to 500 ps. (c) Histogram of the statistical distribution of each voltage. The mean and RMS values of each voltage are listed in Table I.

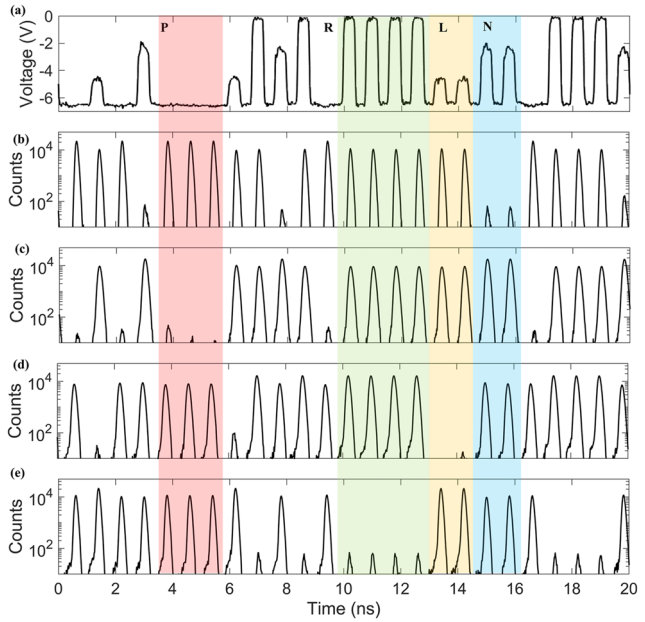


FIG. 7. Polarization states modulation results. (a) Random drive signal output by the chip under the 1.25 GHz clock. (b)–(e) Photon counts of four single photon detectors 1–4.

in Fig. 5, the amplified signal was directly applied to a QKD PIC. The specific PIC utilized in this experiment is a polarization-encoded QKD transmitter.[38] However, our chip can drive any QKD PIC with a 50 ω impedance. The encoded photons were attenuated using a variable optical attenuator (VOA) and subsequently decoded by a BB84 decoding module. Figures 7(b)–7(e) display the coincidence counts recorded by the four single photon detectors over a duration of 20 ns, while Fig. 7(a) represents the corresponding driving signal. In Figs. 7(b) and 7(c), the X basis is represented, whereas Figs. 7(d) and 7(e) represent the Z basis. The high pulse, low pulse, medium pulse, and no pulse were utilized to prepare P, N, L, and R polarization states, respectively. For instance, the high pulses, denoted in pink, encode P polarization states. The number of detected photons for a P-state pulse in detectors 1 and 2 are 22 000 and 18, respectively, resulting in a polarization extinction ratio (PER) exceeding 30 dB. Additionally, detectors 3 and 4 detected roughly the same number of photons for a P-state, half as many as detector 1, indicating that the prepared P-state exhibits a high PER and is perfectly perpendicular to the Z basis. By counting all the encoded pulses, distinguishing the different quantum states, and calculating the PER, we determined that the average PER for the four states is 28.4, 25.0, 26.7, and 25.0 dB, respectively, resulting in an ultra-low source quantum bit error rate (QBER) of 0.24%. This result is indicated by the red dot in Fig. 1(b). It is evident that the designed driver chip significantly enhances the ESNR and reduces the QBER to an exceptionally low level.

TABLE I. Statistics results.

	No. amplification		Amplification			Modulation	
Pulse type	Mean (V)	RMS (V)	Mean (V)	RMS (V)	ESNR (dB)[a]	PER (dB)	QBER (%)
No pulse	−0.062	0.027	−0.265	0.089	18.7	26.7	0.21
Low pulse	−0.441	0.033	−2.412	0.114	17.6	25.0	0.32
Medium pulse	−0.756	0.053	−4.648	0.097	18.3	25.0	0.32
High pulse	−1.414	0.059	−6.545	0.078	19.2	28.4	0.14

[a]ESNR = $10 * \log_{10}$(Mean of the high pulse/RMS).

06 October 2023 01:32:00

Published under an exclusive license by AIP Publishing

IV. CONCLUSION AND DISCUSSION

We introduce an integrated circuit designed for driving electro-optical modulators in QKD systems, specifically for the preparation of quantum states. This circuit is fabricated using 0.18 μm SiGe BiCMOS technology, with a compact chip size of 1.35 × 2.25 mm^2. The chip demonstrates exceptional performance, providing 1.25 GHz multi-amplitude pulse signals with minimal jitter and noise for QKD applications. By utilizing this chip to drive a silicon photonic QKD chip, we achieve remarkable results including a high polarization extinction ratio for quantum state preparation and a low quantum bit error rate at a clock frequency of 1.25 GHz. Integration of our chip into practical QKD systems holds the potential to significantly enhance clock frequency and communication performance.

In future research, the following tasks can be pursued for optimization. First, heterogeneous integration and co-packaging of the driving chip and silicon photonic chip will be investigated to enhance the integration of the QKD transmitter. In addition, chip performance will be further enhanced to support higher frequency QKD systems. This will involve optimizing the chip design scheme as well as exploring alternative fabrication and packaging technologies. The application of our driver chips can extend beyond QKD to other areas, such as classical optical communications. Therefore, we will broaden our research and explore additional scenarios for their utilization.

ACKNOWLEDGMENTS

The authors would like to acknowledge the Information Science Laboratory Center of USTC for the hardware and software services and the Heavy Ion Research Facility in Lanzhou for the support of chip development. This work was supported by the National Key Research and Development Program of China (Grant Nos. 2020YFA0309703, 2020YFA0309701, 2020YFE0200600, and 2022YFF0610100); the Shanghai Municipal Science and Technology Major Project (Grant No. 2019SHZDZX01); and the Innovation Program for Quantum Science and Technology (Grant No. 2021ZD0300104).

AUTHOR DECLARATIONS

Conflict of Interest

The authors have no conflicts to disclose.

Author Contributions

Zhao-Yuan Chen: Data curation (lead); Formal analysis (lead); Writing – original draft (equal). **Chen-Xi Zhu**: Data curation (equal); Writing – original draft (equal). **Zhi-Sheng Huang**: Data curation (supporting). **Yang Li**: Conceptualization (equal); Supervision (equal). **Xin-Zhe Wang**: Conceptualization (equal); Data curation (equal); Supervision (lead); Writing – review & editing (lead). **Fu-Tian Liang**: Resources (equal); Supervision (supporting). **Ge Jin**: Supervision (equal). **Wen-Qi Cai**: Project administration (equal). **Sheng-Kai Liao**: Project administration (lead); Resources (lead); Supervision (equal). **Cheng-Zhi Peng**: Resources (equal).

DATA AVAILABILITY

The data that support the findings of this study are available from the corresponding authors upon reasonable request.

APPENDIX: QBER CALCULATION

The QBER in Fig. 1(b) is calculated based on a Mach–Zehnder modulator driven by a noisy electrical signal. At a given time, this noisy electrical signal can be considered a random variable that obeys a Gaussian distribution, as depicted in Fig. 6(c). The probability distribution density of the voltage V is

$$f_V(V) = \frac{1}{\sqrt{2\pi}\sigma} \exp\left(-\frac{(V - V_0)^2}{2\sigma^2}\right), \tag{A1}$$

where V_0 is the mean value of the signal and σ is the root mean square value of the noise. The ESNR can be expressed as

$$\mathrm{ESNR} = 10 \lg (V_m/\sigma), \tag{A2}$$

where V_m is the maximum voltage amplitude. Here, we only consider the modulation of 0 and π phases, so V_m is the half-wave voltage of the modulator.

The relationship between the voltage and its modulated phase φ is determined by the characteristics and parameters of the modulator. For example, a lithium niobate crystal modulator satisfies a linear relationship. Here, we use the simulation results of the silicon photonics carrier depletion modulator and get the results by fitting a three-order polynomial,

$$\varphi(V) = a_0 + a_1 V + a_2 V^2 + a_3 V^3, \tag{A3}$$

where $a_0 = 0, a_1 = 1.41, a_2 = -0.19$, and $a_3 = 0.02$. According to the density transformation formula, the probability density of the phase φ is

$$f_\varphi(\varphi) = f_V(V(\varphi))|V'(\varphi)|, \tag{A4}$$

where $V(\varphi)$ is the inverse function of $\varphi(V)$, $V(\varphi) = \varphi^{-1}(V)$.

In a polarization encoded QKD frame, the QBER can be directly calculated by the deviation angle $\alpha(\alpha = \varphi/2)$ depicted in Fig. 1(c). Hence, the QBER can be presented as

$$\mathrm{QBER} = \int \sin^2\left(\frac{\phi}{2}\right) f_\varphi(\varphi) d\varphi. \tag{A5}$$

According to Eqs. (A2) and (A5), the numerical relationship between QBER and ESNR can be calculated. Since the voltage and phase relationship in Eq. (A3) is nonlinear, different operating voltages have different tolerances to signal noise. In Fig. 1(b), the QBER and ESNR curve is calculated using $V_0 = 0$ V.

REFERENCES

[1] C. H. Bennett and G. Brassard, in *International Conference on Computer System and Signal Processing ICCSP* (IEEE, 1984), pp. 175–179.
[2] C. H. Bennett, F. Bessette, G. Brassard, L. Salvail, and J. Smolin, J. Cryptol. **5**, 3 (1992).
[3] C. Z. Peng, J. Zhang, D. Yang, W. B. Gao, H. X. Ma, H. Yin, H. P. Zeng, T. Yang, X. B. Wang, and J. W. Pan, Phys. Rev. Lett. **98**, 010505 (2007).

06 October 2023 01:32:00

Published under an exclusive license by AIP Publishing

[4]D. Rosenberg, J. W. Harrington, P. R. Rice, P. A. Hiskett, C. G. Peterson, R. J. Hughes, A. E. Lita, S. W. Nam, and J. E. Nordholt, Phys. Rev. Lett. **98**, 010503 (2007).
[5]H. L. Yin, T. Y. Chen, Z. W. Yu, H. Liu, L. X. You, Y. H. Zhou, S. J. Chen, Y. Mao, M. Q. Huang, W. J. Zhang, H. Chen, M. J. Li, D. Nolan, F. Zhou, X. Jiang, Z. Wang, Q. Zhang, X. B. Wang, and J. W. Pan, Phys. Rev. Lett. **117**, 190501 (2016).
[6]A. Boaron, G. Boso, D. Rusca, C. Vulliez, C. Autebert, M. Caloz, M. Perrenoud, G. Gras, F. Bussières, M.-J. Li, D. Nolan, A. Martin, and H. Zbinden, Phys. Rev. Lett. **121**, 190502 (2018).
[7]Y. Liu, W.-J. Zhang, C. Jiang, J.-P. Chen, C. Zhang, W.-X. Pan, D. Ma, H. Dong, J.-M. Xiong, C.-J. Zhang, H. Li, R.-C. Wang, J. Wu, T.-Y. Chen, L. You, X.-B. Wang, Q. Zhang, and J.-W. Pan, Phys. Rev. Lett. **130**, 210801 (2023).
[8]W. T. Buttler, R. J. Hughes, P. G. Kwiat, S. K. Lamoreaux, G. G. Luther, G. L. Morgan, J. E. Nordholt, C. G. Peterson, and C. M. Simmons, Phys. Rev. Lett. **81**, 3283 (1998).
[9]C.-Z. Peng, T. Yang, X.-H. Bao, J. Zhang, X.-M. Jin, F.-Y. Feng, B. Yang, J. Yang, J. Yin, Q. Zhang, N. Li, B.-L. Tian, and J.-W. Pan, Phys. Rev. Lett. **94**, 150501 (2005).
[10]T. Schmitt-Manderbach, H. Weier, M. Fürst, R. Ursin, F. Tiefenbacher, T. Scheidl, J. Perdigues, Z. Sodnik, C. Kurtsiefer, J. G. Rarity, A. Zeilinger, and H. Weinfurter, Phys. Rev. Lett. **98**, 010504 (2007).
[11]R. Ursin, F. Tiefenbacher, T. Schmitt-Manderbach, H. Weier, T. Scheidl, M. Lindenthal, B. Blauensteiner, T. Jennewein, J. Perdigues, P. Trojek, B. Ömer, M. Fürst, M. Meyenburg, J. Rarity, Z. Sodnik, C. Barbieri, H. Weinfurter, and A. Zeilinger, Nat. Phys. **3**, 481 (2007).
[12]T.-Y. Chen, J. Wang, H. Liang, W.-Y. Liu, Y. Liu, X. Jiang, Y. Wang, X. Wan, W.-Q. Cai, L. Ju, L.-K. Chen, L.-J. Wang, Y. Gao, K. Chen, C.-Z. Peng, Z.-B. Chen, and J.-W. Pan, Opt. Express **18**, 27217 (2010).
[13]S. K. Liao, H. L. Yong, C. Liu, G. L. Shentu, D. D. Li, J. Lin, H. Dai, S. Q. Zhao, B. Li, J. Y. Guan, W. Chen, Y. H. Gong, Y. Li, Z. H. Lin, G. S. Pan, J. S. Pelc, M. M. Fejer, W. Z. Zhang, W. Y. Liu, J. Yin, J. G. Ren, X. B. Wang, Q. Zhang, C. Z. Peng, and J. W. Pan, Nat. Photonics **11**, 509 (2017).
[14]Y. Cao, Y. H. Li, K. X. Yang, Y. F. Jiang, S. L. Li, X. L. Hu, M. Abulizi, C. L. Li, W. Zhang, Q. C. Sun, W. Y. Liu, X. Jiang, S. K. Liao, J. G. Ren, H. Li, L. You, Z. Wang, J. Yin, C. Y. Lu, X. B. Wang, Q. Zhang, C. Z. Peng, and J. W. Pan, Phys. Rev. Lett. **125**, 260503 (2020).
[15]D. Bunandar, A. Lentine, C. Lee, H. Cai, C. M. Long, N. Boynton, N. Martinez, C. Derose, C. Chen, M. Grein, D. Trotter, A. Starbuck, A. Pomerene, S. Hamilton, F. N. Wong, R. Camacho, P. Davids, J. Urayama, and D. Englund, Phys. Rev. X **8**, 021009 (2018); arXiv:1708.00434.
[16]M. Sasaki, M. Fujiwara, H. Ishizuka, W. Klaus, K. Wakui, M. Takeoka, S. Miki, T. Yamashita, Z. Wang, A. Tanaka, K. Yoshino, Y. Nambu, S. Takahashi, A. Tajima, A. Tomita, T. Domeki, T. Hasegawa, Y. Sakai, H. Kobayashi, T. Asai, K. Shimizu, T. Tokura, T. Tsurumaru, M. Matsui, T. Honjo, K. Tamaki, H. Takesue, Y. Tokura, J. F. Dynes, A. R. Dixon, A. W. Sharpe, Z. L. Yuan, A. J. Shields, S. Uchikoga, M. Legré, S. Robyr, P. Trinkler, L. Monat, J.-B. Page, G. Ribordy, A. Poppe, A. Allacher, O. Maurhart, T. Länger, M. Peev, and A. Zeilinger, Opt. Express **19**, 10387 (2011).
[17]J. Yin, Y. Cao, Y. H. Li, S. K. Liao, L. Zhang, J. G. Ren, W. Q. Cai, W. Y. Liu, B. Li, H. Dai, G. B. Li, Q. M. Lu, Y. H. Gong, Y. Xu, S. L. Li, F. Z. Li, Y. Y. Yin, Z. Q. Jiang, M. Li, J. J. Jia, G. Ren, D. He, Y. L. Zhou, X. X. Zhang, N. Wang, X. Chang, Z. C. Zhu, N. L. Liu, Y. A. Chen, C. Y. Lu, R. Shu, C. Z. Peng, J. Y. Wang, and J. W. Pan, Science **356**, 1140 (2017).
[18]S. K. Liao, W. Q. Cai, W. Y. Liu, L. Zhang, Y. Li, J. G. Ren, J. Yin, Q. Shen, Y. Cao, Z. P. Li, F. Z. Li, X. W. Chen, L. H. Sun, J. J. Jia, J. C. Wu, X. J. Jiang, J. F. Wang, Y. M. Huang, Q. Wang, Y. L. Zhou, L. Deng, T. Xi, L. Ma, T. Hu, Q. Zhang, Y. A. Chen, N. L. Liu, X. B. Wang, Z. C. Zhu, C. Y. Lu, R. Shu, C. Z. Peng, J. Y. Wang, and J. W. Pan, Nature **549**, 43 (2017).
[19]S. K. Liao, W. Q. Cai, J. Handsteiner, B. Liu, J. Yin, L. Zhang, D. Rauch, M. Fink, J. G. Ren, W. Y. Liu, Y. Li, Q. Shen, Y. Cao, F. Z. Li, J. F. Wang, Y. M. Huang, L. Deng, T. Xi, L. Ma, T. Hu, L. Li, N. L. Liu, F. Koidl, P. Wang, Y. A. Chen, X. B. Wang, M. Steindorfer, G. Kirchner, C. Y. Lu, R. Shu, R. Ursin, T. Scheidl, C. Z. Peng, J. Y. Wang, A. Zeilinger, and J. W. Pan, Phys. Rev. Lett. **120**, 030501 (2018).
[20]J. Yin, Y. H. Li, S. K. Liao, M. Yang, Y. Cao, L. Zhang, J. G. Ren, W. Q. Cai, W. Y. Liu, S. L. Li, R. Shu, Y. M. Huang, L. Deng, L. Li, Q. Zhang, N. L. Liu, Y. A. Chen, C. Y. Lu, X. B. Wang, F. Xu, J. Y. Wang, C. Z. Peng, A. K. Ekert, and J. W. Pan, Nature **582**, 501 (2020).
[21]Y. Li, S.-K. Liao, Y. Cao, J.-G. Ren, W.-Y. Liu, J. Yin, Q. Shen, J. Qiang, L. Zhang, H.-L. Yong, J. Lin, F.-Z. Li, T. Xi, L. Li, R. Shu, Q. Zhang, Y.-A. Chen, C.-Y. Lu, N.-L. Liu, X.-B. Wang, J.-Y. Wang, C.-Z. Peng, and J.-W. Pan, Optica **9**, 933 (2022).
[22]I. Mammadov, J. Scharnagl, R. Haber, and K. Schilling, in Proceedings of the 73th International Astronautical Congress, 2022.
[23]H. Podmore, I. D'Souza, J. Cain, T. Jennewein, B. L. Higgins, Y. S. Lee, A. Koujelev, D. Hudson, and A. McColgan, in *International Conference on Space Optics—ICSO 2020*, edited by B. Cugny, Z. Sodnik, and N. Karafolas (International Society for Optics and Photonics SPIE, 2021), Vol. 11852, p. 118520H.
[24]A. Villar, A. Lohrmann, X. Bai, T. Vergoossen, R. Bedington, C. Perumangatt, H. Y. Lim, T. Islam, A. Reezwana, Z. Tang, R. Chandrasekara, S. Sachidananda, K. Durak, C. F. Wildfeuer, D. Griffin, D. K. L. Oi, and A. Ling, Optica **7**, 734 (2020).
[25]Y. A. Chen, Q. Zhang, T. Y. Chen, W. Q. Cai, S. K. Liao, J. Zhang, K. Chen, J. Yin, J. G. Ren, Z. Chen, S. L. Han, Q. Yu, K. Liang, F. Zhou, X. Yuan, M. S. Zhao, T. Y. Wang, X. Jiang, L. Zhang, W. Y. Liu, Y. Li, Q. Shen, Y. Cao, C. Y. Lu, R. Shu, J. Y. Wang, L. Li, N. L. Liu, F. Xu, X. B. Wang, C. Z. Peng, and J. W. Pan, Nature **589**, 214 (2021).
[26]H. K. Lo, M. Curty, and B. Qi, Phys. Rev. Lett. **108**, 130503 (2012); arXiv:1109.1473.
[27]A. Boaron, B. Korzh, R. Houlmann, G. Boso, D. Rusca, S. Gray, M.-J. Li, D. Nolan, A. Martin, and H. Zbinden, Appl. Phys. Lett. **112**, 171108 (2018).
[28]R. Sax, A. Boaron, G. Boso, S. Atzeni, A. Crespi, F. GrÜnenfelder, D. Rusca, A. Al-Saadi, D. Bronzi, S. Kupijai, H. Rhee, R. Osellame, and H. Zbinden, Photonics Res. **11**, 1007 (2022); arXiv:2211.11560.
[29]K. Wen, K. Tamaki, and Y. Yamamoto, Phys. Rev. Lett. **103**, 170503 (2009); arXiv:0806.2684.
[30]K. Inoue, E. Waks, and Y. Yamamoto, Phys. Rev. Lett. **89**, 037902 (2002).
[31]D. Stucki, C. Barreiro, S. Fasel, J.-D. Gautier, O. Gay, N. Gisin, R. Thew, Y. Thoma, P. Trinkler, F. Vannel, and H. Zbinden, Opt. Express **17**, 13326 (2009).
[32]D. Stucki, N. Brunner, N. Gisin, V. Scarani, and H. Zbinden, Appl. Phys. Lett. **87**, 194108 (2005).
[33]D. Sadot, G. Dorman, A. Gorshtein, E. Sonkin, and O. Vidal, Opt. Express **23**, 991–997 (2015).
[34]T. K. Paraïso, I. De Marco, T. Roger, D. G. Marangon, J. F. Dynes, M. Lucamarini, Z. Yuan, and A. J. Shields, npj Quantum Inf. **5**, 42 (2019).
[35]X. Zhong, J. Hu, M. Curty, L. Qian, and H. K. Lo, Phys. Rev. Lett. **123**, 100506 (2019).
[36]Z. Yan, E. Meyer-Scott, J. P. Bourgoin, B. L. Higgins, N. Gigov, A. MacDonald, H. Hübel, and T. Jennewein, J. Lightwave Technol. **31**, 1399 (2013).
[37]X. Liu, M. Q. Huang, H. Min, G. Jin, X. Jiang, and C. Z. Peng, Rev. Sci. Instrum. **91**, 024705 (2020).
[38]C. X. Zhu, Z. Y. Chen, Y. Li, X. Z. Wang, C. Z. Wang, Y. L. Zhu, F. T. Liang, W. Q. Cai, G. Jin, S. K. Liao, and C. Z. Peng, Phys. Rev. Appl. **17**(6), 64034 (2022).
[39]T. K. Paraïso, T. Roger, D. G. Marangon, I. De Marco, M. Sanzaro, R. I. Woodward, J. F. Dynes, Z. Yuan, and A. J. Shields, Nat. Photonics **15**, 850 (2021).
[40]K. Wei, W. Li, H. Tan, Y. Li, H. Min, W.-J. Zhang, H. Li, L. You, Z. Wang, X. Jiang, T.-Y. Chen, S.-K. Liao, C.-Z. Peng, F. Xu, and J.-W. Pan, Phys. Rev. X **10**, 031030 (2020); arXiv:1911.00690.
[41]P. Sibson, J. E. Kennard, S. Stanisic, C. Erven, J. L. O'Brien, and M. G. Thompson, Optica **4**, 172 (2017).
[42]L. Schares, J. Kash, F. Doany, C. Schow, C. Schuster, D. Kuchta, P. Pepeljugoski, J. Trewhella, C. Baks, R. John, L. Shan, Y. Kwark, R. Budd, P. Chiniwalla, F. Libsch, J. Rosner, C. Tsang, C. Patel, J. Schaub, R. Dangel, F. Horst, B. Offrein, D. Kucharski, D. Guckenberger, S. Hegde, H. Nyikal, C.-K. Lin, A. Tandon, G. Trott, M. Nystrom, D. Bour, M. Tan, and D. Dolfi, IEEE J. Sel. Top. Quantum Electron. **12**, 1032 (2006).
[43]S. P. Voinigescu, *High-Frequency Integrated Circuits (The Cambridge RF and Microwave Engineering Series)* (Cambridge University Press, 2013).
[44]R. Schmid, T. Meister, M. Rest, and H. M. Rein, Electron. Lett. **34**, 1095 (1998).
[45]C. Knochenhauer, J. C. Scheytt, and F. Ellinger, IEEE J. Solid-State Circuits **46**, 1137 (2011).

06 October 2023 01:32:00

Published under an exclusive license by AIP Publishing

[46]M. Rickelt and H.-M. Rein, IEEE J. Solid-State Circuits **2**, 1184 (2002).
[47]H.-M. Rein, R. Schmid, P. Weger, T. Smith, T. Herzog, and R. Lachner, IEEE J. Solid-State Circuits **29**, 1014 (1994).
[48]R. Schmid, T. F. Meister, M. Rest, and H.-M. Rein, IEEE J. Solid-State Circuits **34**, 886 (1999).
[49]Y. Zhu, X. Wang, C. Zhu, Z. Chen, Z. Huang, Z. Jin, Y. Li, F. Liang, L. Shengkai, C. Peng, and G. Jin, AIP Adv. **12**, 125025 (2022).
[50]N. Hosseinzadeh, A. Jain, K. Ning, R. Helkey, and J. F. Buckwalter, in *2019 IEEE MTT-S International Microwave Symposium (IMS)* (IEEE, 2019), pp. 774–777.
[51]M. Rickelt, H.-M. Rein, and E. Rose, IEEE Trans. Electron Devices **48**, 774 (2001).

06 October 2023 01:32:00

Published under an exclusive license by AIP Publishing